Boundary effects in confined copolymer system and compressible SCFT model

Weiquan Xu, Pingwen Zhang *

School of Mathematical Sciences, Peking University, Beijing 100871, China

ARTICLE INFO

ABSTRACT

The conventionally used Modified Self-consistent Field Theory (MSCFT) for confined system is known to have two major difficulties: numerical instability and dependence on artificial constraints. Here we use Compressible Model based Self-consistent Field Theory (CMSCFT), which has no artificial constraints, and furthermore overcomes numerical instability problems. CMSCFT asymptotically converges to the conventional Self-consistent Field Theory (SCFT) as the compressibility tends to zero. Satisfactory simulations on some hard-surface confinements, focusing on one-dimensional situation, are also given. We suggest that CMSCFT will be a promising tool for copolymer systems with hard surface confinements.

1. Introduction

Self-assembly behavior of block polymers is an effective and efficient method to create structures at nanometer scale which encourages various potential applications including lithographic templates for nano-wires, photonics crystals, and high-density magnetic storage media [1]. As a consequence, block polymers have been the focus of academic community in the past decades. Until recently, plenty of great improvements have been achieved and SCFT is proved to be one of the most powerful tools that successfully characterizes block copolymer melt system without confinements [2–5].

However, things become much more complicated when we consider confinement effects which can influence self-assembly behaviors in the bulk [6,7]. Asakura and Oosawa [8] suggested long ago that the loss of configurational entropy of polymers in the proximity to the hard wall should lead to a strong steric repulsion called "entropy repulsion", giving rise to the depletion of density profile near the hard surface. Furthermore, the competition between the packing constraints and the loss of configurational entropy in the vicinity of the hard wall leads to more complicated polymer interfacial behavior, e.g. surface depletion [9,10], surface density oscillation [11,12], and surface segregation [13]. Thus, the behavior of polymer melts at hard surfaces requires much more efforts than simple liquids. And in this article, we actually focus only on the surface depletion effect, because of the limitation of underlying Gaussian chain copolymer model.

Confinement effects of copolymer melt are also associated with many scientific challenges and technological applications [14], and have drawn increasing interest in the community. The interest in this field can be dated back to 1979, when Joanny et al. first obtained the density profile of polymer solutions [15] by mean-field theory. This result was later confirmed by Allain's direct optical observation, and the profile is shown to be expressed as the square of a hyperbolic tangent [9]:

$$\rho(x) = \tanh^2\left(\frac{x}{\delta}\right), \tag{1}$$

* Corresponding author. Tel.: +86 10 62759851; fax: +86 10 62751801.
 E-mail address: pzhang@pku.edu.cn (P. Zhang).

where δ is the depletion layer thickness. It is striking to note that, Eq. (1) is exactly the same as the profile established by Van der Waals for the interface between the coexisting fluid phases of a binary mixture in 1894 [16]. Later on, J.N. Israelachvili and coworkers performed measurements of equilibrium surface force of various systems, including two samples of liquid polybutadienes (PB) with about $n \approx 20$ and $n \approx 65$ segments [12]. According to Israelachvili et al., the PB samples show steeply repulsive force: effectively an impenetrable "hard wall" at $D \approx 3.0$ nm and $D \approx 3.7$ nm, respectively. These results reveal much important information about surface force of confined copolymer melt systems, though the force law in the area closer to $D = 0$, e.g. $D \in (0, 3$ nm$)$, has not been established yet. A review of recent experimental work about polymer-induced forces near hard surfaces was also given by Kleshchanok et al. [17], where a few theoretical work about surface potential was mentioned as well. In Kleshchanok's review, the Derjaguin approximation [18,19] is highly regarded as a powerful tool computing potential near more complicated surfaces, e.g. sphere and cylinder.

Simultaneously, plenty of computational simulations were also devoted to confinement effects. Monte Carlo simulations were first studied by Kikuchi and Binder [20]. Later, Matsen developed a Modified Self-consistent Field Theory (MSCFT) for confined copolymer systems [21]. In the framework of the conventional SCFT, incompressibility constraint requires the total polymer segmental density to be uniform (normalized as 1 in volume fraction). However, hard wall constraint requires the polymer density to vanish at the surface. In Ref. [21], Matsen generalized this incompressibility condition, and enforced the total segment density to an arbitrarily designed profile ϕ_0 which continuously increases from 0 to 1 in the vicinity of the boundary. This method has been widely used in the subsequent research: Geisinger et al. used cosine-shape profile to examine the phase stability [22]; Chen and Fredrickson adopted a linear profile in ABC triblock thin film [23]; Li et al. chose a "step-function" profile under cylinder confinement [24]. Unfortunately, this widely used method has some inherent problems, such as numerical instability as well as the incorporation of arbitrary profiles. Although Q. Wang et al. recently tried to amend the method under thin film confinement by selecting a "best" profile that reduces numerical instability, they still fail to handle artificiality in density profile and boundary layer thickness [25]. Furthermore, a general approach for the selection of appropriate density profiles in more complicated cases, such as copolymers with different typological structures or as copolymers confined under complex geometries like triangles and pentagrams, is still unknown. In light of these difficulties, we propose this CMSCFT, in the hope that it can be a useful improvement to the current theory.

In the present paper, we use Helfand's harmonic penalty function [26] in compressible SCFT framework, and give some satisfactory simulations on hard-surface confinements. We should mention that, this idea is inspired from the compressible model of homopolymer solution in Fredrickson's monograph [27]. All parameters in CMSCFT have clear physical backgrounds. Boundary potentials can be constructed through physical analysis and experimental inspiration from Israelachvili et al. [28,12,17]. Although we cannot physically determine the model compressibility $1/\zeta$, it is possible to choose an appropriate one by comparing numerical simulations and experimental measurements. We would like to state here that, density profile ϕ_0 is solved self-consistently in CMSCFT. In addition, numerical instability is successfully avoided by using fully implicit numerical solvers for chain propagators. As a consequence CMSCFT should be more flexible for various confined copolymer systems. And furthermore, the boundary layer profile from our simulations has good agreement with experimental results [9] and empirical formula (1). With all above advantages, we suggest that CMSCFT should be a favorable tool for confined copolymer systems. The rest of this article is organized as follows: in Section 2, we deduce Compressible model; in Section 3 we discuss relative algorithm and numerical method; Section 4 shows numerical results of the CMSCFT calculations, where comparison with relative works is also given; finally, concluding remarks are given in Section 5.

2. Compressible model

Suppose the AB diblock copolymer melt system, called $\boldsymbol{R}$, has n copolymers which are described as Gaussian chains $\boldsymbol{r}_j(s)$ with $j = 1, 2, \ldots, n$. We use N to represent the total number of segments per copolymer, and use f to describe copolymer composition: $s \in [0, f]$ for A segments and the rest for B segments. And $\rho_0 = \frac{nN}{V}$ is the total segment density, where V is the system volume. So normalized segment density operators can be written as:

$$\hat{\rho}_A(\boldsymbol{r}) = \frac{N}{\rho_0} \sum_{j=1}^{n} \int_0^f ds \delta(\boldsymbol{r} - \boldsymbol{r}_j(s)),$$
$$\hat{\rho}_B(\boldsymbol{r}) = \frac{N}{\rho_0} \sum_{j=1}^{n} \int_f^1 ds \delta(\boldsymbol{r} - \boldsymbol{r}_j(s)), \tag{2}$$

where $\hat{\rho}_A(\boldsymbol{r})$ and $\hat{\rho}_B(\boldsymbol{r})$ are segment density for A and B, respectively. The Hamiltonian in this system includes both elastic potential energy of Gaussian chain $U_0[\boldsymbol{R}]$ and short-range interaction between AB segments $U_1[\boldsymbol{R}]$, as given below:

$$\beta U_0[\boldsymbol{R}] = \frac{3}{2Nb^2} \sum_{j=1}^{n} \int_0^1 ds \left| \frac{d\boldsymbol{r}_j(s)}{ds} \right|^2,$$
$$\beta U_1[\boldsymbol{R}] = \rho_0 \chi \int d\boldsymbol{r} \hat{\rho}_A \hat{\rho}_B, \tag{3}$$

where we assume that A and B particles have the same statistical segment length b and χ is the Flory–Huggins interaction parameter between segments of different type. Incompressibility in the conventional SCFT framework requires uniform total density: $\hat{\rho}_A(\boldsymbol{r}) + \hat{\rho}_B(\boldsymbol{r}) = 1$ throughout the system, which is ensured by a δ-functional in the partition function.

$$Z = \int \prod_{j=1}^{n} \mathcal{D}\boldsymbol{r}_j \cdot \delta[\hat{\rho}_A + \hat{\rho}_B - 1] \cdot \exp\left\{ -\frac{H\{\boldsymbol{R}\}}{k_B T} \right\}. \tag{4}$$

In order to satisfy the hard wall constraint, Matsen constrained the total density to be a designed profile ϕ_0 by a modified δ-functional [21]:

$$Z = \int \prod_{j=1}^{n} \mathcal{D}\boldsymbol{r}_j \cdot \delta[\hat{\rho}_A + \hat{\rho}_B - \phi_0] \cdot \exp\left\{ -\frac{H\{\boldsymbol{R}\}}{k_B T} \right\}. \tag{5}$$

In CMSCFT, we use Helfand's harmonic penalty function [26] instead to characterize incompressibility:

$$\beta U_2[\boldsymbol{R}] = \frac{1}{2} \zeta \rho_0 \int d\boldsymbol{r} \left(\hat{\rho}_A + \hat{\rho}_B - 1 \right)^2. \tag{6}$$

Note that $1/\zeta$ is the measurement of compressibility: the system becomes incompressible when $1/\zeta \rightarrow 0$. Generally, the energy of polymer–boundary interaction is written as integration of given boundary potential $J(\boldsymbol{r})$:

$$\beta U_3[\boldsymbol{R}] = \frac{\rho_0}{N} \int d\boldsymbol{r} \left(\hat{\rho}_A + \hat{\rho}_B \right) \cdot J(\boldsymbol{r}). \tag{7}$$

The boundary potential $J(\boldsymbol{r})$ is diverging at the vicinity of hard-surfaces. As illustrated latter in this paper, we use the well-known Lennard-Jones potential (23) to describe the interaction between copolymer and hard-surfaces. Now the system Hamiltonian has two more terms than the conventional case:

$$H\{\boldsymbol{R}\} = U_0[\boldsymbol{R}] + U_1[\boldsymbol{R}] + U_2[\boldsymbol{R}] + U_3[\boldsymbol{R}]. \tag{8}$$

And the partition function of compressible model can be written as functional integration without δ-functional:

$$Z = \int \prod_{j=1}^{n} \mathcal{D}\boldsymbol{r}_j \cdot \exp\left\{ -\frac{H\{\boldsymbol{R}\}}{k_B T} \right\}. \tag{9}$$

The field-based Hamiltonian of compressible model can be obtained through a Hubbard–Stratonovich transformation. Interested readers are referred to, e.g., Refs. [5,27] for detailed derivation. Consequently, the field-theoretic Hamiltonian of compressible model can be fixed as follows, up to an unimportant constant which makes no difference of the SCFT model:

$$\frac{H[\mu_+, \mu_-]}{n} = \frac{1}{V} \left[\frac{1}{\chi N} \int d\boldsymbol{r} \mu_-^2 - \int d\boldsymbol{r} \mu_+ \right] - \ln Q\left[w_A, w_B \right] + \frac{1}{V[\chi N + 2\zeta N]} \int d\boldsymbol{r} \left\{ 2J(\boldsymbol{r}) \cdot \mu_+ - \mu_+^2 \right\}, \tag{10}$$

where μ_+ is the fluctuation pressure field, μ_- is the exchange chemical potential field, and $Q[w_A, w_B]$ is the single-chain partition function under conjugate fields w_A and w_B on the A, B segments:

$$w_A = \mu_+ - \mu_-, \qquad w_B = \mu_+ + \mu_-. \tag{11}$$

At the same time, field based partition function can be written as:

$$Z = \int \mathcal{D}\mu_+ \mathcal{D}\mu_- \cdot \exp\left\{ -\frac{H[\mu_+, \mu_-]}{k_B T} \right\}. \tag{12}$$

Please note that, if we consider a free system without boundary influence ($J(\boldsymbol{r}) = 0$), the Hamiltonian of compressible model (10) asymptotically converges in the limit $1/\zeta \rightarrow 0$:

$$\frac{H[\mu_+, \mu_-]}{n} \rightarrow \frac{1}{V} \left[\frac{1}{\chi N} \int d\boldsymbol{r} \mu_-^2 - \int d\boldsymbol{r} \mu_+ \right] - \ln Q\left[\mu_+, \mu_- \right],$$

where the right hand side of the above formula is exactly the field-theoretic Hamiltonian of the conventional SCFT (regardless of a constant shift). Some numerical evidence is added latter in Section 3 as well.

More generally speaking, boundary potential $J(\boldsymbol{r})$ on segment A, B should be different. Thus the energy of polymer–boundary interaction is written as:

$$\begin{aligned} \beta U_3[\boldsymbol{R}] &= \frac{\rho_0}{N} \int d\boldsymbol{r} \left[\hat{\rho}_A \cdot J_A(\boldsymbol{r}) + \hat{\rho}_B \cdot J_B(\boldsymbol{r}) \right] \\ &= \frac{\rho_0}{N} \int d\boldsymbol{r} \left[(\hat{\rho}_A + \hat{\rho}_B) \cdot J_+(\boldsymbol{r}) + (\hat{\rho}_A - \hat{\rho}_B) \cdot J_-(\boldsymbol{r}) \right], \end{aligned} \tag{13}$$

where $J_+(\boldsymbol{r})$ and $J_-(\boldsymbol{r})$ are just notations for convenience:

$$J_+(\boldsymbol{r}) = \frac{J_A(\boldsymbol{r}) + J_B(\boldsymbol{r})}{2}, \qquad J_-(\boldsymbol{r}) = \frac{J_A(\boldsymbol{r}) - J_B(\boldsymbol{r})}{2}.$$

By using a same procedure as above, we can write down the Hamiltonian for compressible model, up to a constant shift:

$$
\begin{aligned}
\frac{H[\mu_+, \mu_-]}{n} &= \frac{1}{V}\left\{\frac{1}{\chi N}\int d\boldsymbol{r}\left[\mu_-^2 + 2J_-(\boldsymbol{r})\cdot\mu_-\right] - \int d\boldsymbol{r}\mu_+\right\} - \ln Q\left[w_A, w_B\right] \\
&\quad + \frac{1}{V[\chi N + 2\zeta N]}\int d\boldsymbol{r}\left\{2J_+(\boldsymbol{r})\cdot\mu_+ - \mu_+^2\right\}.
\end{aligned}
\tag{14}
$$

3. Algorithm

In SCFT, evaluating equilibrium states of copolymer segmental density is equivalent to evaluating the most probable state according to the Boltzmann distribution. For the benefit of convenience, we introduce $F[\mu_+, \mu_-] = H[\mu_+, \mu_-]/n$ as free energy functional. Saddle point approximation reveals that free energy functional $F[\mu_+, \mu_-]$ is to be maximized along pressure field μ_+, and meanwhile to be minimized along exchange chemical potential field μ_-. We use the well-known steepest update strategy to approximate the saddle point. And variational gradients of free energy functional are calculated as follows:

$$
\begin{aligned}
\frac{\delta F[\mu_+, \mu_-]}{\delta\mu_+} &= \frac{2}{V[\chi N + 2\zeta N]}\left[J_+(\boldsymbol{r}) - \mu_+\right] + \frac{1}{V}\left[\rho_A + \rho_B - 1\right], \\
\frac{\delta F[\mu_+, \mu_-]}{\delta\mu_-} &= \frac{1}{V}\left\{\frac{2}{\chi N}\left[\mu_- + J_-(\boldsymbol{r})\right] + \rho_B - \rho_A\right\},
\end{aligned}
\tag{15}
$$

where ρ_A, ρ_B are real density of A, B segments respectively. They can be computed by integrating backward and forward chain propagators $q^+(\boldsymbol{r}, s)$, and $q(\boldsymbol{r}, s)$:

$$
\begin{aligned}
\rho_A &= \frac{V}{Q}\int_0^f ds\, q(\boldsymbol{r}, s)q^+(\boldsymbol{r}, 1-s), \\
\rho_B &= \frac{V}{Q}\int_f^1 ds\, q(\boldsymbol{r}, s)q^+(\boldsymbol{r}, 1-s), \\
Q &= \int d\boldsymbol{r}\, q(\boldsymbol{r}, s)q^+(\boldsymbol{r}, 1-s), \quad \forall s \in [0, 1].
\end{aligned}
\tag{16}
$$

Chain propagators are statistical weight of (sN)th segment located at point $\boldsymbol{r}$, assuming that one of the end segment is uniformly distributed over space ($q^+(\boldsymbol{r}, 0) = 1$, $q(\boldsymbol{r}, 0) = 1$). And these propagators are solutions to the following partial differential equations:

$$
\begin{aligned}
\frac{\partial q(\boldsymbol{r}, s)}{\partial s} &= \Delta_r q(\boldsymbol{r}, s) - w_A(\boldsymbol{r})q(\boldsymbol{r}, s), \quad s \leqslant f, \\
\frac{\partial q(\boldsymbol{r}, s)}{\partial s} &= \Delta_r q(\boldsymbol{r}, s) - w_B(\boldsymbol{r})q(\boldsymbol{r}, s), \quad s > f, \\
\frac{\partial q^+(\boldsymbol{r}, s)}{\partial s} &= \Delta_r q^+(\boldsymbol{r}, s) - w_B(\boldsymbol{r})q^+(\boldsymbol{r}, s), \quad s \leqslant f, \\
\frac{\partial q^+(\boldsymbol{r}, s)}{\partial s} &= \Delta_r q^+(\boldsymbol{r}, s) - w_A(\boldsymbol{r})q^+(\boldsymbol{r}, s), \quad s > f.
\end{aligned}
\tag{17}
$$

Because of the diverging boundary potential, we first apply a change of variable in (15) to avoid excessive numerical error:

$$
\begin{aligned}
\frac{\delta F[\mu_+, \mu_-]}{\delta\tilde{\mu}_+} &= \frac{-2}{V[\chi N + 2\zeta N]}\tilde{\mu}_+ + \frac{1}{V}\left[\rho_A + \rho_B - 1\right], \\
\frac{\delta F[\mu_+, \mu_-]}{\delta\tilde{\mu}_-} &= \frac{1}{V}\left[\frac{2}{\chi N}\tilde{\mu}_- + \rho_B - \rho_A\right], \\
\tilde{\mu}_+ &= \mu_+ - J_+(\boldsymbol{r}), \qquad \tilde{\mu}_- = \mu_- + J_-(\boldsymbol{r}).
\end{aligned}
\tag{18}
$$

Solving the modified diffusion equation of chain propagators efficiently and accurately is crucial in SCFT calculations. As a matter of fact, most computational time is used to solve the PDE of chain propagators. Because of the diverging boundary potential and consequently diverging conjugate fields $\omega(\boldsymbol{r})$, the value of propagators close to the boundary

vanishes automatically and quickly as the contour parameter 's' increases. For simplicity, we apply the Homogeneous Dirichlet condition $q(\mathbf{r}, 0)|_{\mathbf{r} \in \partial \Omega} = 0$, $q^+(\mathbf{r}, 0)|_{\mathbf{r} \in \partial \Omega} = 0$ in this paper. Meanwhile, initial values for the propagators are set as $q(\mathbf{r}, 0)|_{\mathbf{r} \in \Omega / \partial \Omega} = 1$, $q^+(\mathbf{r}, 0)|_{\mathbf{r} \in \Omega / \partial \Omega} = 1$.

As mentioned previously, conjugate fields w_A, w_B are extreme singular near hard surfaces, which is the main challenge in confined systems. The first step to solve this challenge is to design an effective numerical scheme. The most efficient algorithm currently used is the fourth-order method first used by Cochran et al. [29]:

$$\frac{25}{12}q_{n+1} - 4q_n + 3q_{n-1} - \frac{4}{3}q_{n-2} + \frac{1}{4}q_{n-3} = \delta s \cdot [\Delta q_{n+1} - w \cdot (4q_n - 6q_{n-1} + 4q_{n-2} - q_{n-3})]. \tag{19}$$

It is important to note that, in this fourth-order scheme, the term with conjugate field is treated explicitly. In copolymer melt systems without confinements, periodic structures are studied and thus spectral/pseudo-spectral method is preferred. In this case, explicit treatment in (19) has the benefit of computing convolution directly and consequently solving PDE (17) by integrating a system of ordinary differential equations. On the other hand, in copolymer melt systems with hard surface confinements, the singularity of conjugate fields near surface requires this explicit scheme to use an extremely small time step δs for the stability reason. This stability requirement forces δs decreases very quickly as the mesh for space variable '$\mathbf{r}$' become finer. An extremely small time step δs here means solving PDE very inefficiently, however not necessary accurately. Again, because of the singularity of conjugate fields near surface, total segment density distribution raise from zero to one in a very narrow region called boundary layer near hard surfaces. Meanwhile, spectral/pseudo-spectral method is not a good choice for sharp profiles because an extremely large number of base functions are needed. Consequently, there is no reason for the explicit treatment of the term with conjugate fields. And we modify the fourth-order scheme as follows:

$$\frac{25}{12}q_{n+1} - \delta s \cdot \Delta q_{n+1} + \delta s \cdot w \cdot q_{n+1} = 4q_n - 3q_{n-1} + \frac{4}{3}q_{n-2} - \frac{1}{4}q_{n-3}. \tag{20}$$

With this scheme, we can use a reasonable time step size $\delta s \approx 0.01$ just as which usually set in copolymer systems without confinement.

One of the most important advantages of real space methods, e.g. finite difference or finite element method, is the possibility of using non-uniform mesh. When describing sharp profiles, a large number of grid points are needed in a very narrow boundary layer. As a result, an impracticable large number of grid points for the whole domain are needed if uniform mesh is used. On the other hand, non-uniform mesh could greatly reduce the grid points needed. Within a single iteration in SCFT calculation, a common spacial mesh for $q(\mathbf{r}, s)$, $q^+(\mathbf{r}, s)$, $\forall s \in [0, 1]$ is preferred, for the reason that propagators are used to calculate density distributions $\rho_A(\mathbf{r})$, $\rho_B(\mathbf{r})$ as stated in (16). As a result, we do not apply self-adaptive Finite Element Method for the PDE of propagators (17) directly. However, in the light of self-adaptive technique in the Finite Element Method, we use the following indicator for mesh adjustments:

$$\eta_E = \int_{\partial E} h_f \left[\frac{\partial \rho_A}{\partial n} \right]^2 + \int_{\partial E} h_f \left[\frac{\partial \rho_B}{\partial n} \right]^2$$
$$h_{n+1}(E) = \frac{h_n(E)}{f_n(\eta_E)} \tag{21}$$

where E is the element of the mesh, h_f is the scale of the face on element E, η_E is the local indicator for mesh adjustment, $h_n(E)$ is the previous mesh size, $h_{n+1}(E)$ is the new mesh size, $f_n(\eta_e) = \min\{2, \max[1/2, \eta_E/(c \cdot \eta^*)]\}$ is used to determine whether to refine/coarse current element, η^* is the average of η_E for all elements, and c is a constant usually set close to one.

Before going further into the discussion of numerical behavior of previously mentioned algorithm, we would like to have a short discussion on the calculation of free energy. Accurate evaluation of free energy is also crucial in SCFT calculations. However, diverging boundary potential $J(\mathbf{r})$ in (14) brings another challenge for numerical integrations. Fortunately, free energy in SCFT is used to evaluate the thermodynamic stability of given phases. In other words, the only important thing here is the free energy difference among different phases. Furthermore any constant shift in free energy functional (14) can be safely ignored. Consequently, we apply a change of variable in (14) to overcome this challenge and a new free energy functional can be stated as follows up to a constant:

$$\tilde{F}[\tilde{\mu}_+, \tilde{\mu}_-] = \frac{1}{V} \left\{ \frac{1}{\chi N} \int d\mathbf{r} \tilde{\mu}_-^2 - \frac{1}{\chi N + 2\zeta N} \int d\mathbf{r} \tilde{\mu}_+^2 - \int d\mathbf{r} \tilde{\mu}_+ \right\} - \ln Q[w_A, w_B],$$
$$\tilde{\mu}_+ = \mu_+ - J_+(\mathbf{r}), \qquad \tilde{\mu}_- = \mu_- + J_-(\mathbf{r}).$$

According to variational gradients of free energy functional in (18), fields $\tilde{\mu}_+$, $\tilde{\mu}_-$ are not singular. Now, accurate free energy can be easily calculated.

In order to discuss the numerical behavior of this recommended algorithm, we fix the relative parameters as $\chi N = 12$, $f = 0.48$, $\zeta N = 120$, $L = 1.2\pi$. According to our calculation, full implicit fourth-order scheme (20) is stable even when the time step is set quite large as $\delta s = 0.04$. Stability here means smooth profiles for calculated propagators $q(\mathbf{r}, s)$, $q^+(\mathbf{r}, s)$ and densities $\phi_A(\mathbf{r})$, $\phi_B(\mathbf{r})$, and smooth convergence of steepest decent iteration where L_∞ norm of variational gradients of
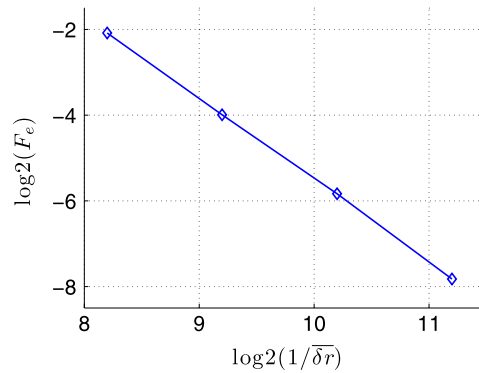
Fig. 1. Second-order accuracy of free energy calculation, along space discretization. Here $\overline{\delta r} = L/DOF$ represents the average element scale (L is the film thickness, DOF is the number of grid points) and F_e represents the error of free energy (comparing to that calculated from the finest mesh with $\delta s = 10^{-3}$, $\overline{\delta r} \approx 10^{-4}$). In these calculations, $\delta s = 10^{-3}$, and $DOF = 550 \times 2, 550 \times 2^2, 550 \times 2^3, 550 \times 2^4$ for data points marked by diamonds from the left to the right respectively.
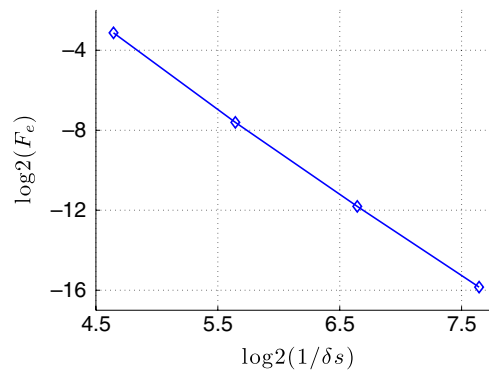
Fig. 2. Fourth-order accuracy of free energy calculation, along chain contour discretization. Here F_e represents the error of free energy (comparing to that calculated from the finest mesh with $\delta s = 10^{-3}$, $\overline{\delta r} \approx 10^{-4}$). In these calculations, space discretization is fixed as $DOF = 550 \times 2^4$ thus $\overline{\delta r} \approx 10^{-4}$, and $\delta s = 0.04, 0.02, 0.01$ and 0.005 for data points marked by diamonds from the left to the right respectively.

free energy decays lower than 10^{-4} while the update of free energy smaller than 10^{-6} within hundreds of steepest decent iterations. At the same time, non-uniform grids show its virtue in hard surface confinement with sharp boundary profiles. By using around 550 grid points, the relative error of calculated free energy, comparing to that calculated from much denser mesh, is lower than 0.1. Furthermore, when we refine the mesh, we get fourth-order accuracy along chain contour direction 's' as a result of the fourth-order scheme (20), and get second-order accuracy along space direction '$\mathbf{r}$' owing to linear finite element base function is used. To evaluate the order of accuracy, we fix the time step $\delta s = 10^{-3}$ and in the first step use mesh adjustment strategy (21) resulting in a non-uniform mesh with around 550 grid points, then we apply global refinement to this mesh for more accurate calculation of free energy. In the next step, we fix the finest non-uniform space mesh with about 35,000 grid points to evaluate the accuracy along chain contour direction 's', time step is set to $\delta s = 0.04, 0.02, 0.01$ and 0.005 respectively. This result is shown in Figs. 1 and 2, where we introduce some notations: $\overline{\delta r} = L/DOF$ represents the average element scale (L is the film thickness, DOF is the number of grid points) and F_e represents the error of free energy (comparing to that calculated from the finest mesh with $\delta s = 10^{-3}$, $\overline{\delta r} \approx 10^{-4}$). From these two figures, we clearly observe a fourth-order accuracy along chain contour direction 's', and a second-order accuracy along space direction. We would like to note here that, higher order of accuracy along space direction is possible if higher order of base functions are used in the finite element method.

4. Results and discussion

For simplicity, our simulation only considers lamellae phase of diblock copolymer melt thin films, which can be reduced to a 1-D case. We note that, all simulations can be directly applied to 3-D case without difficulty but would require much more computational effort. The parameters are fixed as follows in the simulation, unless mentioned otherwise:

$$\varepsilon_{AA} = \varepsilon_{BB} = 0.1, \qquad \varepsilon_{AB} = 0.2; \qquad N = 120, \qquad f = 0.48, \qquad L = 4\pi \cdot R_g, \tag{22}$$

where, L is the thickness of thin films and R_g is polymer's unperturbed radius of gyration. Note that SCFT involves multi-solutions. All those equilibrium states we get from simulations should be meta-stable phase that relies significantly on initial
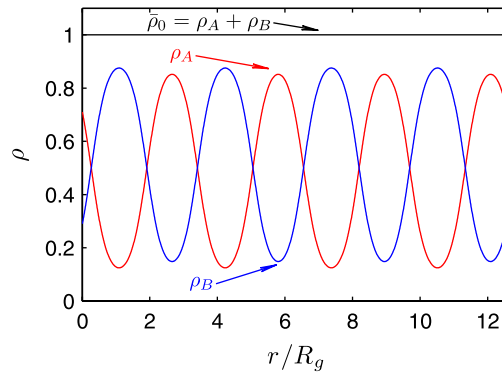
Fig. 3. Density profiles for lamellae phase without hard wall confinement. ρ_A denotes density of A-segments, ρ_B for B-segments, and $\bar{\rho}_0$ for total density of all segments.
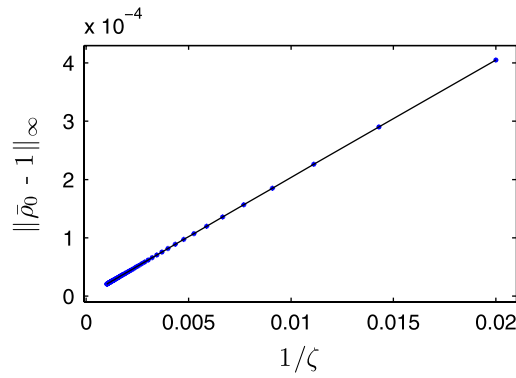
Fig. 4. Total density $\bar{\rho}_0$ of CMSCFT converges to 1 when ζ tends to ∞.

fields we provide beforehand. In the following simulations, we set $\mu_+ = 0$, $\mu_- = 1$ which has no inclination to any special density profile pattern.

4.1. Model comparison

As shown in the previous section, CMSCFT without confinement asymptotically converges to the conventional SCFT when compressibility $1/\zeta$ drops to zero. Numerical simulation confirms this result as well. Periodic boundary condition is applied here and boundary potential in CMSCFT was set to be zero: $J(\mathbf{r}) = 0$. Fig. 3 shows the density profiles of the conventional SCFT. Just as expected, little difference between density profile of the two models was noticed even when incompressibility is only about $\zeta = 10$. Furthermore, from Fig. 4 we can observe a clear linear dependence that shows precisely how CMSCFT asymptotically converges to the conventional SCFT in the limit $1/\zeta \to 0$:

$$\|\bar{\rho}_0 - 1\|_\infty = C \cdot \frac{1}{\zeta},$$

where $\bar{\rho}_0 = \rho_A + \rho_B$ is the total density of both segments.

### 4.2. Confinement effects and boundary layer

Confinement effects, such as density depletion, surface oscillation, and surface segregation, have generated increasing interests in the community. Although plenty of efforts have been made, there are still lots of work to do. As stated in Section 1., the conventionally used MSCFT skill developed by Matsen [21] is not very satisfactory. Moreover, no method has been proposed to calculate boundary layer thickness in numerical simulations. In this section, we are going to show that CMSCFT gives a satisfactory simulation of density depletion and chain end enrichment. Furthermore, boundary layer profile and thickness are calculated self-consistently in CMSCFT.

4.2.1. Surface depletion

Equilibrium surface force measurement of two liquid PB samples by Israelachvili et al. [12] shows no oscillation but steeply repulsive force approaching the boundaries. For this kind of system, the modified Lennard-Jones potential is
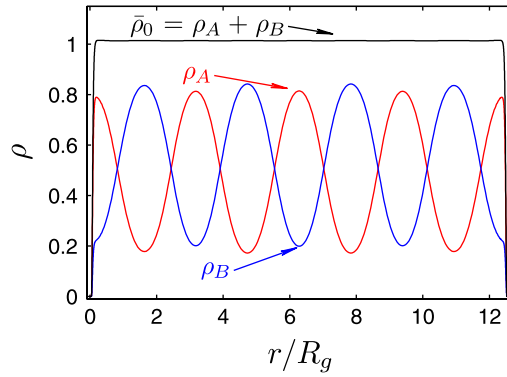
Fig. 5. Density profiles for lamellae phase with hard wall confinement, where the Lennard-Jones potential (24) is used and ζ is set to be 10. Notations are used the same as Fig. 3.
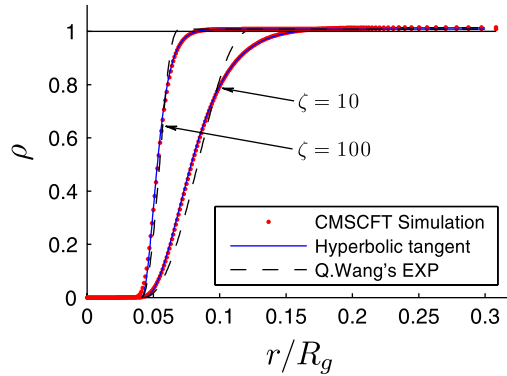
Fig. 6. Boundary layer profile near hard surface. Again, the Lennard-Jones potential (24) is used and ζ is set to be 10, 100 respectively. Comparison with empirical Hyperbolic tangent (1) and Q. Wang's EXP in MSCFT [25] is given with the same layer thickness. (For interpretation of the references to color in this figure legend, the reader is referred to the web version of this article.)

appropriate to characterize the hard wall influence:

$$J(\mathbf{r}) = \begin{cases} 4\alpha \left[\left(\dfrac{\sigma}{d(\mathbf{r})} \right)^{12} - \left(\dfrac{\sigma}{d(\mathbf{r})} \right)^{6} \right] + \alpha & d(\mathbf{r}) \leqslant \sqrt[6]{2}\sigma \\ 0 & \text{otherwise,} \end{cases} \tag{23}$$

where $d(\mathbf{r})$ is the distance of the point $\mathbf{r}$ to boundary. Note that polymer–boundary interaction only happens when segments are adjacent to the boundary. And $b = \sqrt{6/N}R_g$ is the statistical segment length in Gaussian chain model of block copolymer. Consequently, we can fix $\sigma = b/2$ in Eq. (23), e.g., $\sigma \sim 0.1R_g$ when $N = 120$ and $b \approx 0.22R_g$. Finally, α in (23) is fixed to control the magnitude of the Lennard-Jones potential. Surface interaction energy is $\sim k_BT$ according to Israelachvili's measurement [30,12]. Hence we simply set $\alpha = 1$ here. Specifically, the following Lennard-Jones potential is used in our calculation for convenience:

$$J(\mathbf{r}) = \begin{cases} 4 \cdot \left[\left(\dfrac{0.1}{d(\mathbf{r})} \right)^{12} - \left(\dfrac{0.1}{d(\mathbf{r})} \right)^{6} \right] + 1 & d(\mathbf{r}) \leqslant 0.1 \times \sqrt[6]{2} \\ 0 & \text{otherwise.} \end{cases} \tag{24}$$

Fig. 5 shows density profiles of the confined system. By comparing with Fig. 3, we note that, hard wall confinement does not change the pattern of density profile in the bulk. Fig. 6 illustrates the profile of boundary layer. The red dots are the simulations of CMSCFT, the blue line is the empirical formula (1), and the dotted line is Q. Wang's exponential profile for the "best" numerical behavior. Note that all three profiles share the same boundary layer thickness δ in this manner:

$$\delta = \int_0^{\mathbf{r}_0} (\psi - \rho(\mathbf{r})) \, d\mathbf{r}, \tag{25}$$

where ψ, a constant, is the total density in the bulk where far enough away from boundaries, $\rho(\mathbf{r})$ is the total polymer density, and '$\mathbf{r}_0$' is a distance far away from boundaries where polymer density reach bulk density: $\rho(\mathbf{r}_0) = \psi$. Boundary layer
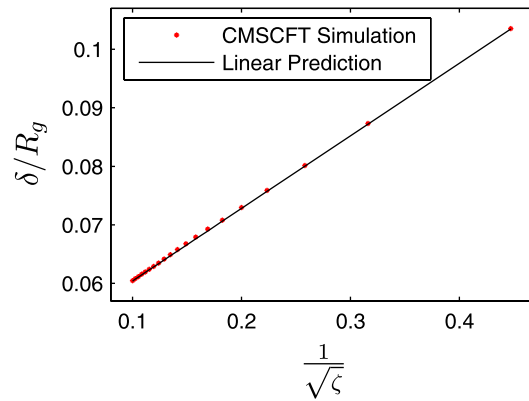
Fig. 7. Layer thickness $\delta - \zeta$ dependence. Comparison between CMSCFT simulation and linear prediction (26) is given. Note that here the specified Lennard-Jones (24) is used.
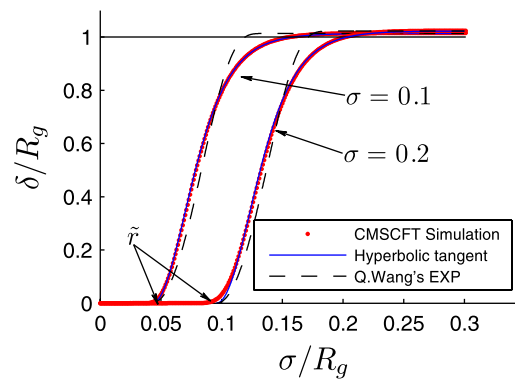

Fig. 8. Boundary Layer $-\sigma$ dependence. ζ is set to be 10. Comparison with empirical Hyperbolic tangent (1) and Q. Wang's EXP in MSCFT [25], in the condition of a same layer thickness, is given.

thickness, according to formula (25), is $\sim 0.09 R_g$ and $0.06 R_g$ respectively. From Fig. 6, we note that CMSCFT simulation perfectly matches the empirical Hyperbolic tangent profile (1).

4.2.2. Boundary layer thickness

Boundary layer thickness is also very important in various applications. In current simulation methods, such as Monte-Carlo and MSCFT, boundary layer thickness was set artificially. On the contrary, CMSCFT can automatically determine the layer thickness with the given boundary potential. The relationships between layer thickness and various parameters in CMSCFT are investigated. Again, the Lennard-Jones potential (23) is used in this section, and formula (25) is served as the definition of layer thickness. We did not see notable influence of parameters: $\chi N, f$, and L. However, a simple dependence of δ on ζ and σ is observed. As shown in Fig. 7, where the specified Lennard-Jones (24) is used and thus $\sigma = 0.1$, there is a simple relationship between δ and ζ:

$$\delta \approx 0.124 \frac{1}{\sqrt{\zeta}} + 0.048; \tag{26}$$

From Fig. 8, we can see that σ in the Lennard-Jones potential (23) hardly influences the shape of Boundary Layer Profile but will linearly affect the position $\tilde{r}$ where total density $\bar{\rho}_0$ starts to increase. Furthermore, we also note that the dependence of δ on ζ and σ can be reasonably written as:

$$\delta = 0.124 \frac{1}{\sqrt{\zeta}} + \frac{\sigma}{2}. \tag{27}$$

In the light of Eq. (27), we can choose an appropriate model compressibility parameter ζ, by comparison with experimental measurements, to make a more reasonable simulation.

4.2.3. Structures and free energy

In this section, we want to study the phase transition behavior with respect to the distance between two hard surfaces (thickness of the thin film L). Again, we use a slightly asymmetry diblock copolymer as mentioned previously (22).
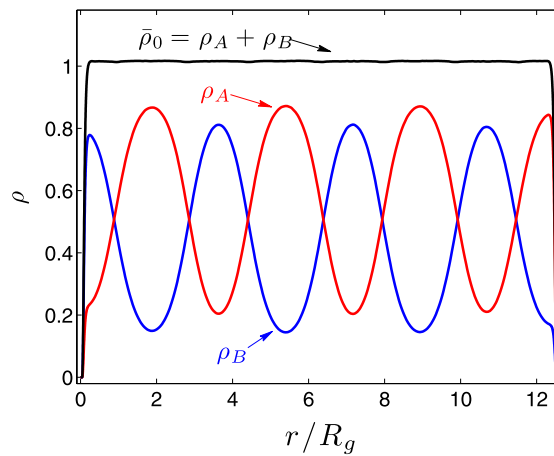
Fig. 9. Density profiles for lamellae phase (Phase-Mix) with hard wall confinement. Notations are used the same as Fig. 3.
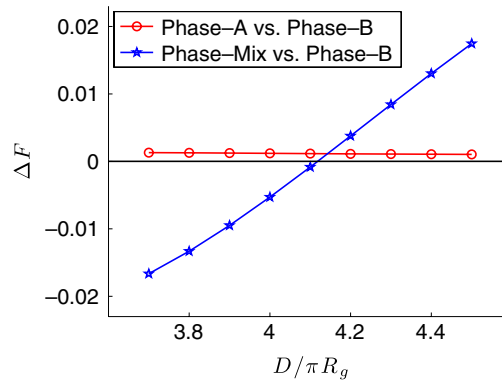

Fig. 10. Free energy difference among different patterns of lamellae structures. Parameters used in the calculation is set as mentioned previously (22). Two curves of free energy difference, Phase-A vs. Phase-B and Phase-Mix vs. Phase-B, are plotted here. A phase transition between Phase-B and Phase-Mix happens at around $L \approx 4.12\pi R_g$.

According to our calculation, we observed three different patterns of lamellae when the film thickness (L) is set around $L \approx 4\pi R_g$. These three different patterns of lamellae are: Phase-A represents the structure shown in Fig. 5, Phase-B represents a similar structure as Phase-A but B domains are located near the surface, Phase-Mix represents the structure shown in Fig. 9, where both A domain and B domain locate near one side of the surface respectively. It can be interesting to study the free energy relationship of these three different structures, Phase-A, Phase-B and Phase-Mix, as the film thickness L changes. In Fig. 10, we plot the free energies of these three structures. To illustrate free energy differences more clearly, instead of plotting free energy curves directly we plot two curves of difference between Phase-A and Phase-B, and between Phase-Mix and Phase-B. From the figure, we can see that the free energy of Phase-A is almost the same as but always slightly higher than that of Phase-B. It is interesting to notice that, when film thickness L is small Phase-Mix has a lowest free energy. And the free energy of Phase-Mix increases observably as L increases. Eventually, when the film thickness L is large enough, Phase-Mix displays a highest free energy of these three structures. From Fig. 10 we can find a phase transition between Phase-B and Phase-Mix, which happens at around $L \approx 4.12\pi R_g$. Actually, there is an intuitive interpretation of this result. The key point is that lamellae structure has its optimal period. If the confinement is too narrow and squeezing or on the other hand too wide and stretching the structure, the free energy is much higher and the corresponding structure becomes meta-stable.

5. Conclusion

In this paper, we study Compressible Model based SCFT (CMSCFT) for confined diblock copolymer melt system. The Lennard-Jones potential is used to describe the boundary potential of this hard surface confinement. It might be interesting to note that, without hard surface confinement where boundary potential is zero, CMSCFT converges to conventional SCFT as the compressibility $1/\zeta$ decreases. One of the interesting advantages of CMSCFT is calculating boundary layer profile self-consistently with no artificial constraints. Furthermore, full implicit fourth-order scheme (20) is used to solve chain propagators, which successfully avoid numerical instability and obtain fourth-order accuracy for the calculation of free

energy along chain contour discretization. Non-uniform grids are used with finite element method here to describe the sharp boundary layer near hard surfaces. According to our calculation, this algorithm, full implicit fourth-order scheme and non-uniform grids, provides satisfiable numerical simulations. Specifically speaking, time steps along chain contour parameter 's' can be set fairly large $\delta s \approx 0.01$, and only hundreds of grid points for space variables 'r' are acceptable in one-dimensional calculations. In a word, CMSCFT successfully overcomes the two major difficulties in the conventional Modified Self-consistent Field Theory: numerical instability and dependence on artificial constrains.

We also discuss some interesting calculations of hard surface confined diblock copolymer melt system using CMSCFT. First of all, boundary layer profile of CMSCFT simulations matches perfectly with the empirical Hyperbolic-tangent profile. While the "best" profile proposed by Q. Wang et al., for conventional Modified Self-consistent Field Theory, has a notable difference to that calculated self-consistently by CMSCFT. Secondly, CMSCFT method can conveniently calculate boundary layer thickness, and give the relationship between layer thickness and some model parameters. Finally, we study free energy and corresponding phase behavior of three different patterns of lamella in hard surface confinement. A phase transition is observed as the thin film thickness L changes.

As a final remark: CMSCFT is quite flexible for various confined copolymer systems. Although only one-dimensional calculations in diblock copolymer system is discussed in this paper, extension to more complicated geometries constrains and more complicated architecture copolymer (like triblock and star copolymer) should be straightforward. Consequently, CMSCFT can be a promising tool in confined copolymer system simulations.

Acknowledgments

References

[1] C. Park, J. Yoon, E.L. Thomas, Polymer 44 (2003) 6725–6760.
[2] L. Leibler, Macromolecules 13 (1980) 1602.
[3] A.N. Semenov, Sov. Phys.—JETP 61 (1985) 733.
[4] M.W. Matsen, M. Schick, Phys. Rev. Lett. 74 (1995) 4225.
[5] ANC SHI Developments in Block Copolymer Science and Technology, 2004, pp. 265–293.
[6] Weihua Li, Robert A. Wickham, Robert A. Garbary, Macromolecules 39 (2006) 806–811.
[7] G.J.A. Sevink, A.V. Zvelindovsky, B.A.C. van Vlimmeren, N.M. Maurits, J.G.E.M. Fraaije, J. Chem. Phys. 110 (1999) 2250.
[8] S. Asakura, F. Oosawa, J. Chem. Phys. 22 (1954) 1255.
[9] C. Allain, D. Ausserre, F. Rondelez, Phys. Rev. Lett. 49 (1982) 1694.
[10] J.N. Israelachvili, S.J. Kott, J. Chem. Phys. 88 (1988) 7162;
     R.G. Horn, J.N. Israelachvili, Macromolecules 21 (1988) 2836.
[11] H.K. Christenson, D.W.R. Gruen, R.G. Horn, J.N. Israelachvili, J. Chem. Phys. 87 (1987) 1834.
[12] J.N. Israelachvili, Stephen J. Kott, J. Chem. Phys. 88 (1988) 7162.
[13] M. Sikka, N. Singh, A. Karim, F.S. Bates, Phys. Rev. Lett. 70 (1993) 307.
[14] P.G. de Gennes, Adv. Colloid Interface Sci. 27 (1987) 189;
     S. Wu, PolymerInterfaces and Adhesion, Dekker, New York, 1982.
[15] J.F. Joanny, L. Leibler, P.G. de Gennes, J. Polym. Sci. Polym. Phys. Ed. 17 (1979) 1073.
[16] J.D. van der Waals, Z. Phys. Chem. 13 (1894) 657.
[17] Dzina Kleshchanok, Remco Tuinier, Peter R. Lang, J. Phys.: Condens. Matter 20 (2008) 073101.
[18] B.V. Derjaguin, Kolloidn. Zh. 69 (1934) 155.
[19] J.N. Israelachvili, Intermolecular and Surface Forces, second ed., Academic, London, 1992.
[20] M. Kikuchi, K. Binder, J. Chem. Phys. 101 (1994) 3367; Europhys. Lett. 21 (1997) 427.
[21] M.W. Matsen, J. Chem. Phys. 106 (1997) 7781.
[22] T. Geisinger, M. Müller, K. Binder, J. Chem. Phys. 111 (1999) 5241.
[23] H.Y. Chen, G.H. Fredrickson, J. Chem. Phys. 116 (2002) 1137.
[24] W.H. Li, R.A. Wickham, R.A. Garbary, Macromolecules 39 (2006) 806.
[25] Dong Meng, Qiang Wang, J. Chem. Phys. 126 (2007) 234902.
[26] Eugene Helfand, J. Chem. Phys. 62 (1975) 999.
[27] Glenn H. Fredrickson, The Equilibrium Theory of Inhomogeneous Polymers, Oxford University Press, Oxford, 2006.
[28] R.G. Horn, J.N. Israelachvili, Macromolecules 21 (1988) 2836–2841.
[29] Eric W. Cochran, Carlos J. Carcia-Cerera, Glenn H. Fredrickson, Macromolecules 39 (2006) 2449.
[30] J.N. Israelachvili, G.E. Adams, J. Chem. Soc. Faraday Trans. I 74 (1978) 975.